

Chapter 4

A Time-dependent Spectral Evolution Model

Having calculated the evolution of the fluid quantities and magnetic field in a pulsar wind nebula, the following three chapters will focus on the second aim of this study, namely that of calculating the evolution of a non-thermal particle energy spectrum in such a nebula. While this aim is primarily concerned with developing a spatially dependent particle evolution model, this chapter first presents a spatially independent model, and shows how values for a number of important nebular parameters, such as the ratio of electromagnetic to particle energy, can be derived.

Although largely similar to those developed by, e.g., *Zhang et al.* (2008) and *Tanaka and Takahara* (2010), the model presented in this chapter differs in a number of key aspects. As discussed in Section 2.3.3, observations indicate that the electron¹ spectrum injected into the nebula at the termination shock can be described by a broken power law. In contrast to previous models, the present one allows for the possibility that the source spectrum can have a discontinuity in intensity at the transition between the low- and high-energy components. Another difference is that the present model also allows for the fact that the nebula can be compressed by the reverse shock of the supernova remnant, leading to the electrons gaining energy as a result of adiabatic heating. In order to illustrate the usefulness of the model, it is applied to the nebula G21.5–0.9.

Apart from applying it to the study of known pulsar wind nebulae, the model can also be used to elucidate the nature of the unidentified TeV sources that have been detected by the H.E.S.S. experiment (*Aharonian et al.*, 2008). These sources lack any clear synchrotron counterparts, thereby making their identification difficult. One possibility is that the unidentified sources are ancient pulsar wind nebulae, as will be explained in the next section. Apart from testing the ancient pulsar wind nebula hypothesis, the model is also applied to HESS J1427–608 (*Aharonian et al.*, 2008) and HESS J1507–622 (*Acero et al.*, 2011) in order to determine whether these unidentified TeV sources can be identified as such.

¹The term *electron* is used as a collective term for both electrons and positrons, as it is generally believed that both these particles should be present in equal numbers in PWNe.

The research presented in this chapter has also been published in *Vorster et al.* (2013b).

4.1 Unidentified sources as ancient pulsar wind nebulae

It is well-known that the X-ray synchrotron emission observed from PWNe is produced by a young population of electrons, as these particles have a relatively short lifetime (see, e.g., *Shklovskii*, 1957). The evolution of the X-ray emission is therefore correlated with the evolution of the magnetic field and, following Figures 3.1 and 3.3, with the morphological evolution of the PWN. In contrast, the electrons producing VHE gamma-ray emission have a much longer lifetime, implying that the observed TeV emission from PWNe is produced by particles that have accumulated over the lifetime of the pulsar (see, e.g., *De Jager and Djannati-Ataï*, 2009). This is strikingly illustrated by the energy-dependent morphology of the ~ 21 kyr old nebula HESS J1825–137, where VHE gamma-ray observations reveal a PWN that is significantly larger than the associated X-ray nebula (*Aharonian et al.*, 2006). For a PWN with an average magnetic field of $B = 5 \mu\text{G}$, the lifetime of an electron emitting 1 keV X-rays is ~ 3 kyr, whereas the corresponding lifetime of an electron producing 1 TeV gamma-rays is ~ 19 kyr (see, e.g., *De Jager and Djannati-Ataï*, 2009).

Based on the information presented above, *De Jager* (2008) proposed that the average magnetic field in an older PWN could evolve below the $B \sim 3 \mu\text{G}$ value of the ISM, with the result that these sources would be undetectable at synchrotron frequencies. However, due to the longer lifetimes of the VHE gamma-ray producing electrons, these ancient PWNe may still be visible at TeV energies. As PWNe count among the more common TeV sources, the ancient PWN scenario could offer an explanation for a number of unidentified TeV sources that lack a synchrotron counterpart (*Aharonian et al.*, 2008).

The proposal of *De Jager* (2008) is directly supported by the results of Section 3.3.3, and in particular Figure 3.3, where it is shown that the average magnetic field decreases as $\bar{B} \propto t^{-1.1} - t^{-1.5}$. The magnetic field will thus decrease to a very low level if the time scale required for the reverse shock to reach the PWN is large. Furthermore, if the nebula is not significantly compressed by the reverse shock, the magnetic field will remain weak, resulting in a faint synchrotron source.

4.2 The model

The temporal evolution of the electron spectrum in a PWN can be calculated using the equation (see, e.g., *Tanaka and Takahara*, 2010)

$$\frac{\partial N_e(E_e, t)}{\partial t} = Q(E_e, t) + \frac{\partial}{\partial E} \left[\dot{E}(E_e, t) N_e(E_e, t) \right], \quad (4.1)$$

where E_e represents the electron energy and $N_e(E_e, t)$ the number of electrons per energy interval. The number of electrons injected into the PWN at the termination shock, per time

and energy interval, is given by $Q(E_e, t)$, while the second term on the right-hand side of (4.1) describes continuous energy losses (or gains) suffered by the electrons, with $\dot{E}(E_e, t)$ the total energy loss rate.

Following *Venter and de Jager (2007)*, a broken power-law spectrum is used to model the emission from the sources studied in this chapter,

$$Q(E_e, t) = \begin{cases} Q_R (E_b/E_e), & \text{if } E_{\min} \leq E_e \leq E_b \\ Q_X (E_b/E_e)^2, & \text{if } E_b < E_e \leq E_{\max} \end{cases}, \quad (4.2)$$

where Q_R and Q_X are normalisation constants, E_{\min} and E_{\max} are the minimum and maximum electron energy respectively, and E_b is the energy at which the spectrum transitions between the two components. Note that the indices of (4.2) follow from the discussion presented in Section 2.3.3. Keeping in mind that *De Jager et al. (2008b)* showed that a discontinuous spectrum is a plausible solution for Vela X, it is not an a priori requirement that the two components should have the same intensity at E_b . Both possibilities are thus investigated during the modelling procedure, with the choice ultimately determined by which spectrum leads to a markedly better agreement between the model prediction and data. If both spectra lead to an equally good prediction, this will be clearly pointed out and discussed.

Before continuing, it may be worthwhile to mention that a discontinuous spectrum is generally not used in PWN modelling. However, a motivation for using such a spectrum is discussed in Section 2.3.3, and it is reiterated that this spectrum is not a priori favoured. Furthermore, the discontinuous spectrum is only used as an approximation for a spectrum that, in reality, will be smooth. Lastly, it should also be kept in mind that the two electron components are not necessarily spatially coincident in the nebula (see Section 2.3.3). The model is thus limited in this regard as it is spatially independent.

For a discontinuous source spectrum, the normalisation constants are determined by the prescription that the total energy in a given component should be some fraction η_i ($i = R, X$) of the pulsar's spin-down luminosity $L(t)$ (see, e.g., *Venter and de Jager, 2007*)

$$\int Q_i (E_b/E_e)^{p_i} E_e dE_e = \eta_i L(t). \quad (4.3)$$

For the low-energy component of the spectrum one has $p_R = 1$, and the above integral leads to the expression

$$Q_R = \frac{\eta_R L}{E_b} \frac{1}{(E_b - E_{\min})} \quad (4.4)$$

for the low-energy normalisation constant. In the model the index of the high-energy component is chosen to be $p_X = 2$, and integration of (4.3) leads to

$$Q_X = \frac{\eta_X L}{E_b^2} \frac{1}{\ln(E_{\max}/E_b)} \quad (4.5)$$

for the high-energy normalisation constant.

For a continuous source spectrum, the total energy should again be some fraction η of $L(t)$. However, in this case only a single normalisation constant $Q_0 = Q_R = Q_X$ is required, and is calculated using the expression

$$Q_0 \left[\int_{E_{\min}}^{E_b} \left(\frac{E_b}{E_e} \right) E_e dE_e + \int_{E_b}^{E_{\max}} \left(\frac{E_b}{E_e} \right)^2 E_e dE_e \right] = \eta L. \quad (4.6)$$

Integrating the above expression, and rearranging the variables, leads to the equation

$$Q_0 = \frac{\eta L}{E_b^2} \left[\ln \left(\frac{E_{\max}}{E_b} \right) - \left(\frac{E_{\min}}{E_b} \right) + 1 \right]^{-1}. \quad (4.7)$$

When calculating the normalisation constants for both the discontinuous and continuous source spectra it is assumed that the pulsar is a pure dipole radiator with a braking index of 3, while the time-dependence of $L(t)$ is given by (2.4).

The total energy loss rate \dot{E} in (4.1) includes both synchrotron radiation and IC scattering, as well as adiabatic cooling/heating. The energy loss rate as a result of synchrotron radiation and IC scattering is given by (see, e.g., Longair, 2011)

$$\dot{E}_{n-t}(E_e, t) = \frac{4}{3} \frac{\sigma_T}{(m_e c)^2} E_e^2 U_B \left(1 + \frac{U_{IC}}{U_B} \right), \quad (4.8)$$

where σ_T is the Thomson cross-section and m_e the electron mass. In this non-thermal loss rate

$$U_{IC} = \int_{\epsilon_{\min}}^{\epsilon_{\max}} u_\epsilon d\epsilon \quad (4.9)$$

represents the energy density of the target photon field for inverse Compton scattering, with u_ϵ the energy distribution of these photons, and

$$U_B = \frac{B^2}{8\pi} \quad (4.10)$$

the energy density of the magnetic field. As the model does not include a spatial component, B effectively represents the average magnetic field \bar{B}_{pwn} in the nebula.

Although (4.8) describes IC scattering in the Thomson regime, Moderski *et al.* (2005) have shown that this expression is still valid if $U_{IC}/U_B \lesssim 3$, and Klein-Nishina effects can be neglected. For the CMBR with an energy density of $U_{IC} = 0.3 \text{ eV cm}^{-3}$, this condition is satisfied for an average magnetic field of $\bar{B} > 2 \mu\text{G}$. Anticipating the modelling results, it was however found that this condition is violated for both HESS J1427–608 and HESS J1507–622, and Klein-Nishina effects are taken into account by multiplying (4.8) with a correction factor F_{KN} . Moderski *et al.* (2005) have further shown that when the target photon field is described by a black-body spectrum, the modification factor can be approximated by

$$F_{\text{KN}} \sim \frac{1}{(1 + 4\gamma\epsilon)}, \quad (4.11)$$

where $\gamma = E_e/m_e c^2$ is the Lorentz factor of the electron and $\epsilon = 2.8k_B T/m_e c^2$. In the last expression k_B represents Boltzmann's constant and T the temperature of the black-body spectrum. For modelling purposes it is assumed that the IR and star light photon fields can be described by a black-body spectrum.

For adiabatic cooling (or heating), the energy loss rate is given by

$$\dot{E}_{\text{ad}}(E_e, t) = \frac{1}{3} (\nabla \cdot \mathbf{V}) E_e, \quad (4.12)$$

where \mathbf{V} is the convection velocity downstream of the termination shock. If the system has a spherical symmetry, then (4.12) can be simplified to

$$\dot{E}_{\text{ad}}(E_e, t) = \frac{1}{3r^2} \frac{\partial}{\partial r} [r^2 V(r)] E_e. \quad (4.13)$$

From the above expression it follows that the adiabatic loss rate decreases as a function of radius. Furthermore, the electrons will not be subjected to adiabatic losses if $V \propto 1/r^2$. Therefore, to correctly include adiabatic losses requires not only that $V(r)$ be known, but also a model with a spatial dimension. This will be better illustrated in the next chapter, where a spatially dependent particle evolution model is presented and discussed.

For the present spatially independent model the following approximation is used

$$\dot{E}_{\text{ad}}(E_e, t) = \frac{V_{\text{pwn}}(t)}{R_{\text{pwn}}(t)} E_e, \quad (4.14)$$

where $V_{\text{pwn}}(t)$ and $R_{\text{pwn}}(t)$ are respectively the expansion velocity and radius of the PWN. A similar approximation was also used by *Tanaka and Takahara (2010)* in their spatially independent PWN model.

It was discussed in Section 2.3.2, and illustrated by the hydrodynamic results of Section 3.3.1, that a PWN goes through three evolutionary phases. Based on Figure 3.1 in the above-mentioned section, the expansion/compression of $R_{\text{pwn}}(t)$ in these three phases is approximated using the power laws

$$R_{\text{pwn}}(t) = \begin{cases} R_0(t/t_0)^{r_1} & \text{if } t < t_{\text{rev}} \\ R_0(t_{\text{rev}}/t_0)^{r_1} (t/t_{\text{rev}})^{r_2} & \text{if } t_{\text{rev}} \leq t < t_{\text{sec}} \\ R_0(t_{\text{rev}}/t_0)^{r_1} (t_{\text{sec}}/t_{\text{rev}})^{r_2} (t/t_{\text{sec}})^{r_3} & \text{if } t \geq t_{\text{sec}} \end{cases} \quad (4.15)$$

Here t_{rev} again represents the time needed for the reverse shock of the SNR to reach the PWN, as described by (2.1), and t_{sec} the time when the PWN enters the second expansion phase. Furthermore, compression of the PWN implies that $r_2 < 0$. For the initial condition, $R_0 = 0.01$ pc when $t_0 = 10$ yr (*Gelfand et al., 2009*). The values r_1 , r_2 , and r_3 are not linearly independent, as the size of the PWN predicted by the model must be equal to the observed size. Note that the distance to the source d influences the values of r_1 , r_2 and r_3 , as a larger value of d implies a larger source, and hence a faster expansion.

Apart from R_{pwn} , the adiabatic loss rate (4.14) is also a function of the expansion velocity of the PWN $V_{\text{pwn}}(t) = dR_{\text{pwn}}(t)/dt$. *Gelfand et al. (2009)* calculated that the expansion velocity increases from $V_{\text{pwn}}(t) \sim 1300$ km s⁻¹ at $t = 0.01$ kyr to $V_{\text{pwn}}(t) \sim 2300$ km s⁻¹ at $t = 5$ kyr. However, these values were calculated for a specific scenario, and are only provided as a point of reference. Similar values for $V_{\text{pwn}}(t)$ also follow from Figures 3.1 and 3.4.

The evolution of the average magnetic field in the nebula $\bar{B}_{\text{pwn}}(t)$ is calculated using the conservation of magnetic flux, and is based on the results presented in Section 3.3.3. As an analytical expression for the evolution of R_{pwn} is used, the integral (3.12) can be employed. The same approach was also used by *Tanaka and Takahara* (2010) to calculate the evolution of $\bar{B}_{\text{pwn}}(t)$ in their model. An important parameter introduced in Section 3.3.3 is η_B , defined as the fraction of the pulsar's spin-down luminosity converted into magnetic energy.

As discussed in Section 3.3.5, the ratio of the electromagnetic to particle energy σ plays an important role in PWNe. In terms of the parameters present in the particle evolution model, this ratio is defined as

$$\sigma = \frac{\eta_B}{\eta_R + \eta_X}, \quad (4.16)$$

and is subjected to the constraint $\sigma \lesssim 1$ (see Section 2.3.1). An additional constraint follows from $\eta_B + \eta_R + \eta_X \lesssim 1$. This sum is not set strictly equal to unity to allow for the fact that a fraction η_{rad} of the pulsar's spin-down luminosity is radiated away in the form of pulsed emission, i.e. $\eta_B + \eta_R + \eta_X + \eta_{\text{rad}} = 1$. For the modelling $\eta_{\text{rad}} \lesssim 1\%$ is used, similar to the value derived for the Crab pulsar (see Section 2.2.1). Note that this small value used for η_{rad} effectively implies that $\sigma \simeq \eta_B$.

It is important to note that the hydrodynamic simulations presented in the previous chapter cannot be used a priori to motivate the evolution of $R_{\text{pwn}}(t)$, and consequently that of $V_{\text{pwn}}(t)$ and $\bar{B}_{\text{pwn}}(t)$. This is due to the fact that the hydrodynamic model is only valid when $\sigma < 0.01$, while the particle model has no such limitation.

Apart from energy losses, the model also takes into account that electrons can escape from the PWN as a result of diffusion. The escape time scale τ_{esc} , as derived by *Parker* (1965), is given by

$$\tau_{\text{esc}}(t) = \frac{R_{\text{pwn}}^2(t)}{6\kappa_{\text{Bohm}}(t)}, \quad (4.17)$$

where $\kappa_{\text{Bohm}} = (1/3)VR_G$ is the Bohm diffusion coefficient and

$$R_G = \frac{mV_{\perp}}{qB} \quad (4.18)$$

is the non-relativistic gyroradius of the particle. In the expression above q represents the charge of the particle and V_{\perp} its velocity perpendicular to the magnetic field. The electrons in the PWN are highly relativistic ($V \rightarrow c$), with the relativistic Bohm diffusion coefficient given by

$$\kappa_{\text{Bohm}}(t) = \frac{cE_e}{3qB(t)}. \quad (4.19)$$

The temporal evolution of the electron spectrum is not obtained by solving (4.1) directly, but rather in the following fashion: the amount of electrons with energy E_e injected into the PWN over the time interval dt is given by $Q(E_e, t)dt$, where $Q(E_e, t)$ is specified by (4.2). The injected electrons are then added to the current value of $N_e(E, t)$ to obtain the total number of electrons in the nebula $N_e(E_e, t + dt) = N_e(E_e, t) + Q(E_e, t)dt$. In the time interval dt the electrons

also suffer energy losses as a result of adiabatic cooling and non-thermal radiation. The new electron energy is given by $E'_e = E_e - dE_e$, where dE_e is the sum of the loss rates (4.8) and (4.14). The electrons $N_e(E_e, t + dt)$ will therefore evolve to a new position in energy space $N'_e(E'_e, t + dt)$. During the interval dt a fraction of the electrons will also have escaped from the nebula. Assuming that the electrons are distributed uniformly throughout the nebula, the fraction of electrons escaping from the nebula in the time interval dt is given by $\xi_{\text{esc}} = dt/\tau_{\text{esc}}$, with the escape time scale defined by (4.17). As $\xi_{\text{esc}} \geq 1$ indicates that all electrons have effectively escaped from the system, the length of the time step is chosen in such a fashion so that the condition $\xi_{\text{esc}} \ll 1$ is satisfied. The number of electrons remaining in the nebula after a time $t + dt$ is thus given by $N'_e(E'_e, t + dt)(1 - \xi_{\text{esc}})$. This approach is essentially similar to the those used by, e.g., *Gelfand et al. (2009)*, *Schöck et al. (2010)*, and *Van Etten and Romani (2011)*, and is adequate provided that dt is chosen to be sufficiently small.

In order to determine if the model predicts the correct evolution of the electron spectrum, it was tested using three well-known criteria: (1) adiabatic losses shift the entire spectrum to lower energies without changing the shape of the spectrum; (2) in the absence of synchrotron losses, electrons escaping from a system will result in a softer spectrum, with this softening directly related to the energy dependence of the diffusion coefficient. In the present model $\kappa \propto E_e$, and the spectrum should be softer by one power of E_e compared to the source spectrum; (3) if the system is in a steady-state, synchrotron losses lead to a spectrum that is steeper by one power of E_e when compared to the source spectrum (see, e.g., *Pacholczyk, 1970*). It was found that the model predicts all of the above-mentioned behaviour, as will be discussed in Section 4.3.1. Note that (1) and (2) will be discussed in detail in the next chapter, which focuses on a spatially dependent particle evolution model.

In reality, the evolution of a PWN could be considerably more complex than described by the model. One might, for example, think of a nebula that expands in a very inhomogeneous ISM. Simulations by, e.g., *Blondin et al. (2001)* and *Vorster et al. (2013a)* show that in such a scenario the reverse shock of the SNR will be asymmetric, leading to a cigar or bullet-shaped PWN. One might also argue, with merit, that a more realistic model should include a spatial dependence, like the model presented in the next chapter. However, for the case where only spatially integrated observations are available, it is not clear how useful a spatially dependent model would be. In this regard, the present model should be viewed as a first-order approximation. Furthermore, any time-dependence in the conversion efficiencies η_R , η_X , and η_B , as well as the values of the energy spectrum E_{min} , E_{max} , and E_b , is not taken into account. It is not known if any theoretical calculations exist that predict the time-dependence of these parameters.

The non-thermal emission is calculated using the appropriate expressions given by *Blumenthal and Gould (1970)*. This implies that Klein-Nishina effects are taken into account when calculating the IC spectrum.

One feature of the model is that it contains a number of free parameters which can lead to parameter degeneracies. This is especially true for the candidate nebulae HESS J1427–608 and

HESS J1507–622, as many of the parameter values, e.g., $L(t)$, are not constrained by observations. This problem is further complicated by the fact that no definitive theoretical predictions exist for, e.g., the break energy E_b . A thorough treatment of the problem would therefore require an investigation of the whole possible parameter space. However, even without such an investigation it is nevertheless possible to constrain the parameters to a certain degree.

The largest challenge of spatially independent spectral evolution models is generally related to predicting the correct flux for the multi-wavelength data. In a scenario where the electrons scatter only the CMBR photons the number of electrons present in the nebula can be derived from the GeV and TeV data (*De Jager, 2007*). With the number of electrons known, the magnetic field can be immediately derived from a prediction of the synchrotron data, leading to reasonably unique values for the parameters influencing the flux. Unfortunately this procedure becomes more complicated if other radiation fields are important. Nevertheless, during the modelling process it was found that certain values for the average magnetic field \bar{B} and initial luminosity L_0 are always required in order to predict the observed flux. This will be highlighted when the modelling results for a particular source are discussed.

Lastly, compared to other parameters such as $L(t)$ and τ , the parameters E_{\min} , E_{\max} , and E_b have only a small influence on the flux, and are therefore less critical to the modelling. These parameters are primarily used to improve the model prediction after a reasonable prediction has already been obtained.

4.3 Results

4.3.1 A test-case PWN

It is instructive to first apply the model to a general PWN in order to illustrate the effects that the various free parameters have on the evolution of the non-thermal radiation spectra. For the test case, a PWN is placed at a distance of 1 kpc and is allowed to expand for $t_{\text{age}} = 1$ kyr, with the nebula having a present-day size of $R_{\text{pwn}} = 1$ pc, and an expansion velocity of $V_{\text{age}} = 1000 \text{ km s}^{-1}$. The conversion efficiency of spin-down luminosity to magnetic energy is chosen to be $\eta_B = 0.03$, leading to a present-day magnetic field of $\bar{B}_{\text{age}} = 50 \mu\text{G}$. For this specific PWN, both adiabatic and escape losses are neglected.

The first important distinction that can be made is the effect of a continuous/discontinuous electron spectrum on the broadband emission. Note that both these source spectra are described by (4.2), but with the following difference: for the continuous spectrum the two components of the broken power law have the same intensity at E_b . In the case of the discontinuous spectrum, the intensity of the high-energy component at E_b is below that of the low-energy component. It follows from (4.6) that the continuous spectrum requires only a single conversion efficiency $\eta \equiv \eta_R + \eta_X$. For both the continuous and discontinuous spectra the values

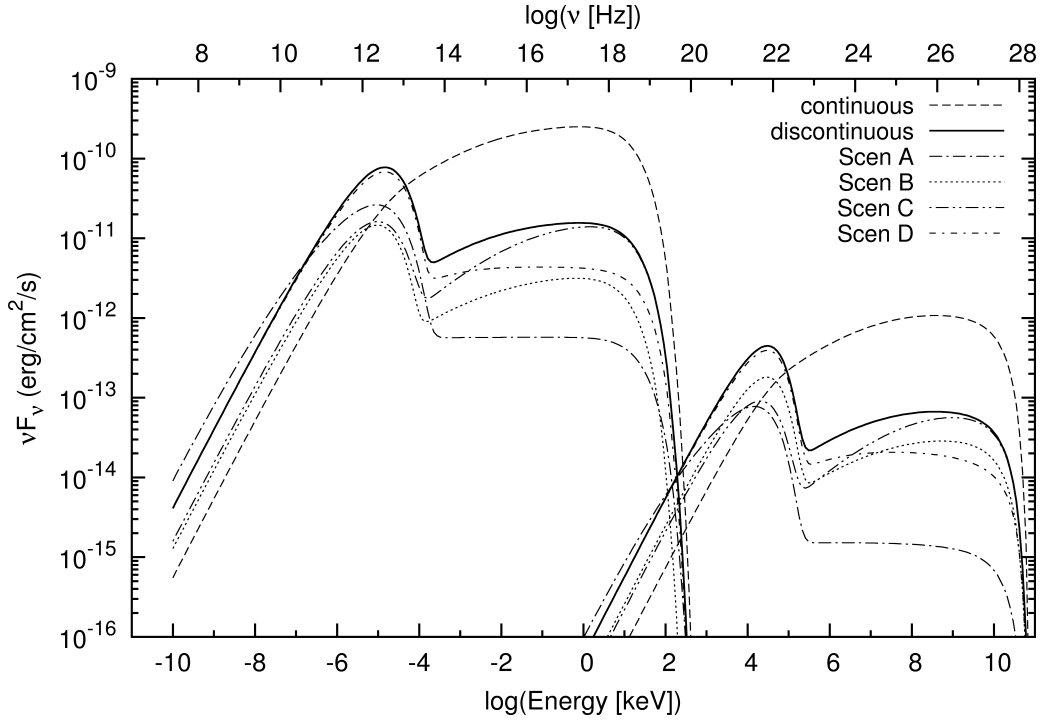


Figure 4.1: Evolution of the non-thermal radiation spectra for a model PWN. The discontinuous spectrum is used as a reference scenario (see text for parameter values used), while Scenarios A–D are identical to the reference scenario, with the exception of one varied parameter. The parameters that were varied are listed in Table 4.1.

$\eta_R = 0.92$ and $\eta_X = 0.05$ are chosen, implying that the same fraction of the pulsar’s spin-down luminosity is converted to electron energy for the two cases.

The radiation spectra obtained with the two types of source spectra are shown in Figure 4.1. This figure shows that the continuity/discontinuity in the electron spectra is preserved in the non-thermal emission. Another salient feature visible in Figure 4.1 is that the different source spectra predict fluxes for the non-thermal emission that differ by more than an order of magnitude. This discrepancy is easy to explain if it is kept in mind that in both scenarios the same amount of spin-down energy is converted to electron energy.

To transform a discontinuous source spectrum into continuous spectrum requires that a fraction of the energy stored in the low-energy component must be transferred to the high-energy component, thereby reducing the intensity of the former, while increasing the intensity of the latter. As the low-energy component is described by $N_e \propto E_e^{-1}$, and the high-energy component by $N_e \propto E_e^{-2}$, a small change in the intensity (or equivalently energy) of the former component will lead to a larger change in the intensity of the latter component. This can also be seen from Figure 4.1, where the discrepancy between the X-ray spectra is larger than the discrepancy between the radio spectra. With these differences taken into account, it is clear that the two source spectra will lead to the derivation of different parameters for the same PWN.

Having demonstrated the effect of the source spectrum on the non-thermal emission, it is also

Table 4.1: Parameter values used for the scenarios depicted in Figure 4.1. The values in brackets indicate the values used for the discontinuous source spectrum scenario.

Scenario	Difference to reference scenario
Scen A	PWN has an age of $t_{\text{age}} = 10 \text{ kyr}$ ($t_{\text{age}} = 1 \text{ kyr}$)
Scen B	spin-down time scale of the pulsar is $\tau = 0.3 \text{ kyr}$ ($\tau = 1 \text{ kyr}$)
Scen C	adiabatic losses are included (adiabatic losses are neglected)
Scen D	escape losses are included (escape losses are neglected)

necessary to demonstrate the effect that different values for the various parameters have on the evolution of the non-thermal spectra. For this purpose a number of alternative scenarios are chosen, with these alternative scenarios having only one varied parameter compared to the discontinuous source spectrum scenario. The parameters varied are listed in Table 4.1, with the quantity in brackets indicating the value of the quantity in question in the reference scenario.

The first quantity varied is the age of the system, corresponding to Scen A in Figure 4.1. Synchrotron and IC losses cause the intensity of the high-energy component to decrease as the PWN ages, while the spectral index becomes steeper by one power of energy. In contrast, the low-energy component remains largely unaffected by non-thermal energy losses. As discussed in Section 4.2, this is the theoretically expected effect of non-thermal losses, thus indicating that the model works correctly.

In the next scenario, Scen B, the spin-down time scale is reduced to $\tau = 0.3 \text{ kyr}$. Figure 4.1 shows that the influence of this parameter is to reduce the intensity of the the non-thermal flux at all wavelengths. When $t \ll \tau$, the spin-down luminosity of the pulsar is approximately constant, but decreases rapidly after $t \gtrsim \tau$. As the number of electrons injected into the nebula is determined by the time integral over L , which in turn is dependent on the value of τ , a smaller number of electrons have been injected into the nebula in Scen B (compared to the reference scenario), leading to the reduced flux.

The next parameter investigated is the effect of adiabatic losses, as shown by Scen C. In contrast to synchrotron and IC losses, adiabatic losses have an influence on the evolution of both the low- and high-energy components of the electron spectrum, and the importance of adiabatic losses at higher energies will ultimately be determined by the strength of the magnetic field. Figure 4.1 shows that with the parameters chosen for the model PWN adiabatic cooling is the dominant energy loss mechanism for energies $E \lesssim 0.1 \text{ keV}$. As a result, the intensity of the spectra at these energies decreases, while the spectral shape remains similar to that of the injection spectrum (see Section 5.2.3). At higher energies ($E \gtrsim 0.1 \text{ keV}$) the effect of synchrotron losses becomes more important, leading to a softening of the spectrum.

Lastly, Scen D shows the effect of escape losses on the radiation spectra. For the purposes of illustration, a diffusion coefficient $\kappa = 500\kappa_{\text{Bohm}}$ is used. As κ scales with energy, the high-energy component of the electron spectrum is primarily affected, leading to a decrease in the

Table 4.2: Values derived with the model for G21.5–0.9 and HESS J1427–608. Values marked with an asterisk represent parameters that were kept fixed, or parameters that follow from the derived model parameters.

Parameter	Symbol	G21.5–0.9 HESS J1427–608		
		Scen A	Scen B	
Initial spin-down luminosity (10^{38} erg s $^{-1}$)	L_0	0.54*	9	9
Spin-down time scale (kyr)	τ	3*	3	3
Age of nebula (kyr)	t_{age}	0.87*	6.4*	6.4*
Present-day average magnetic field (μG)	\bar{B}_{age}	186	3.7	0.3
Radio conversion efficiency	η_{R}	0.75	0.93	0.84
X-ray conversion efficiency	η_{X}	0.13	0.06	0.15
Ratio: electron conversion efficiencies	$\eta_{\text{R}}/\eta_{\text{X}}$	5.7*	15.5*	5.6*
Ratio: magnetic to particle energy (10^{-3})	σ	120*	0.2*	0.001*
Minimum electron energy (10^{-3} TeV)	E_{min}	0.3	100	100
Maximum electron energy (10^2 TeV)	E_{max}	2.7	1.2	1.2
Break energy (TeV)	E_{b}	0.12	0.18	0.18
Distance to source (kpc)	d	4.8*	8	8

Table 4.3: The same as Table 4.2, but for HESS J5107–622. Note that in Scen B the high-energy component of the electron spectrum has an index of $\alpha = 2.7$, in contrast to the value $\alpha = 2$ used for all other scenarios.

Parameter	Symbol	HESS J1507–622		
		Scen A	Scen B	Scen C
Initial spin-down luminosity (10^{38} erg s $^{-1}$)	L_0	0.55	4	8
Spin-down time scale (kyr)	τ	2.5	2.5	0.3
Age of nebula (kyr)	t_{age}	4.6	4.6	14
Present-day average magnetic field (μG)	\bar{B}_{age}	2.4	1	1.9
Electron conversion efficiency	η_{R}	0.95	0.99	—
Radio conversion efficiency	η_{R}	—	—	0.86
X-ray conversion efficiency	η_{X}	—	—	0.12
Ratio: electron conversion efficiencies	$\eta_{\text{R}}/\eta_{\text{X}}$	—	—	7.2*
Ratio: magnetic to particle energy (10^{-3})	σ	40*	1*	9*
Minimum electron energy (10^{-3} TeV)	E_{min}	1	10	10
Maximum electron energy (10^2 TeV)	E_{max}	1	1.3	1
Break energy (TeV)	E_{b}	0.5	0.5	0.5
Distance to source (kpc)	d	6*	6*	6*

intensity of the of the X-ray/TeV spectra, as shown in Figure 4.1. It can also be seen from the figure that escape losses lead to a spectrum that is softer by one power of E_e compared to the source spectrum. Once again, this result shows that the model predicts the correct spectral evolution.

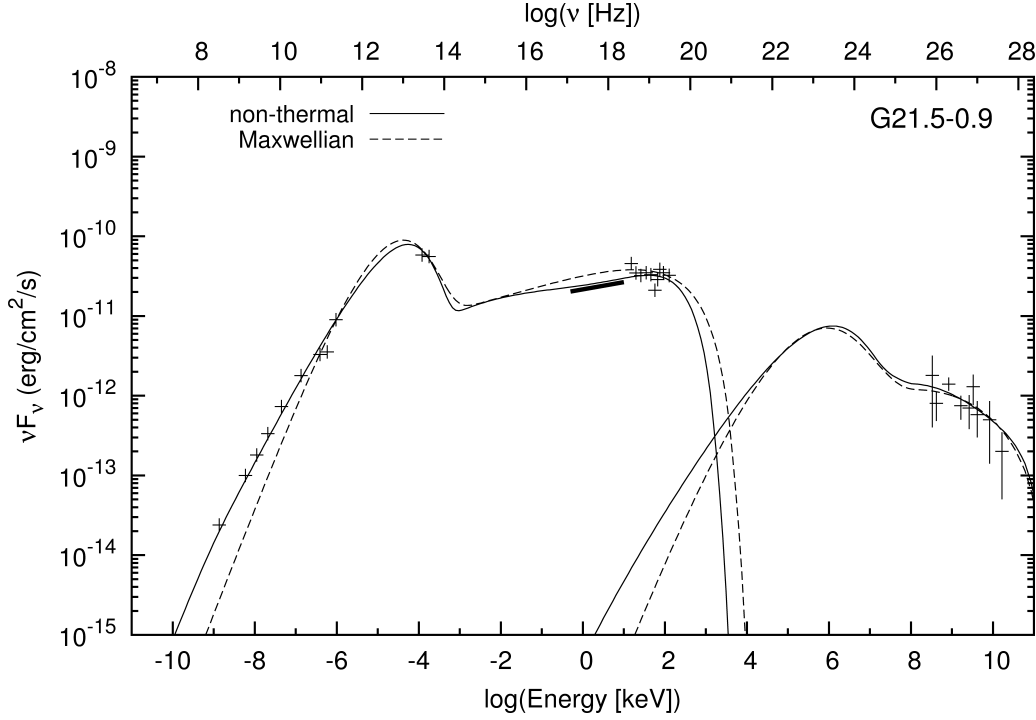


Figure 4.2: Model prediction for the young nebula G21.5–0.9. Radio data are taken from *Goss and Day* (1970), *Becker and Kundu* (1975), *Morsi and Reich* (1987), *Salter et al.* (1989a,b), *Bock et al.* (2001), *Bandiera et al.* (2001), *Bietenholz and Bartel* (2008), and *Bietenholz et al.* (2011), IR data from *Gallant and Tuffs* (1999), X-ray data from *Slane et al.* (2000), *De Rosa et al.* (2009), and the INTEGRAL Science Data Centre (<http://www.isdc.unige.ch/heavenswebapp/integral>), and TeV data from *De Jager et al.* (2008a). The IC prediction is calculated using both the CMBR and an SSC component, although the former component leads to a negligible flux.

4.3.2 G21.5–0.9

With a spin-down luminosity of $L = 3.3 \times 10^{37} \text{ erg s}^{-1}$ (*Camilo et al.*, 2006), the pulsar in the supernova remnant G21.5–0.9 is one of the most energetic pulsars in the Galaxy. The PWN is located at a distance of 4.8 kpc (*Tian and Leahy*, 2008), with an estimated age of $t_{\text{age}} = 870 \text{ yr}$ (*Bietenholz and Bartel*, 2008). Radio (see, e.g., *Goss and Day*, 1970; *Becker and Kundu*, 1975; *Morsi and Reich*, 1987; *Salter et al.*, 1989a,b; *Bock et al.*, 2001; *Bandiera et al.*, 2001; *Bietenholz and Bartel*, 2008; *Bietenholz et al.*, 2011), IR (see, e.g., *Gallant and Tuffs*, 1999; *Zajczyk et al.*, 2012), and X-ray (*Slane et al.*, 2000; *De Rosa et al.*, 2009; *Tsujimoto et al.*, 2011) observations of the PWN show a bright nebula with a radius of $\sim 40''$. The nebula is embedded in diffuse X-ray emission, believed to be the result of dust-scattered X-rays from the PWN (*Bocchino et al.*, 2005). At GeV energies *Fermi-LAT* only detected upper limits for the nebula (*Ackermann et al.*, 2011), while a detection at TeV energies has been reported by the H.E.S.S. collaboration (*Djannati-Atai et al.*, 2007; *De Jager et al.*, 2008a).

For the modelling of G21.5–0.9, a number of constraints on the parameters follow from observations. As the age and present-day luminosity are known, the initial luminosity is fixed for a choice of τ through (2.4). For the spin-down time scale, the value of $\tau = 3 \text{ kyr}$ estimated

by *De Jager et al.* (2009b) is used. The derived distance to the source implies a PWN radius of $R_{\text{pwn}} = 0.93$ pc. The PWN is too young to have interacted with the reverse shock, and must therefore still be in the first expansion phase. With the age and size of the PWN taken into account, the expansion index in (4.15) has the value $r_1 = 1.02$, with the time derivative of (4.15) leading to a present-day expansion velocity of $V_{\text{age}} = 1060 \text{ km s}^{-1}$.

Figure 4.2 shows the model prediction for the non-thermal radiation spectra, with the derived parameters listed in Table 4.2. In order to find an agreement between the TeV data and the model prediction, it is necessary to include synchrotron self-Compton scattering (SSC) in the model. *Atoyan and Aharonian* (1996) calculated that the density of the synchrotron photon field is

$$n_{\text{ssc}} = \frac{Q_{\text{syn}} \bar{U}}{4\pi R_{\text{syn}} c h\nu}, \quad (4.20)$$

where Q_{syn} is the synchrotron emissivity for a given frequency ν , R_{syn} is the radius within which most of the synchrotron emission is produced, and $\bar{U} \simeq 2.24$. Additionally, photons from the CMBR were also taken into account, but it was found that the contribution from this radiation field is negligible compared to the contribution from the SSC component.

Using the model a present-day average magnetic field of $\bar{B}_{\text{age}} = 186 \mu\text{G}$ is derived. This is significantly larger than the value $\bar{B}_{\text{age}} \leq 64 \mu\text{G}$ derived by *Tanaka and Takahara* (2010) for the same nebula. Smaller values for the average magnetic field were thus also investigated, but it was found that it becomes very difficult for the model to predict the observed flux. Larger magnetic field values are, however, possible.

Observations of G21.5–0.9 (see, e.g., *Slane et al.*, 2000; *Bock et al.*, 2001; *Bocchino et al.*, 2005) show a radio and X-ray PWN that are not only spatially coincident, but also have the same size. It is therefore difficult to reconcile the large magnetic field derived from the model with the data as the X-ray producing electrons will have a very short life time, leading to an X-ray PWN that will be much smaller than the radio counterpart. However, it will be shown in the next chapter, specifically Section 5.2.5, that when diffusion is an important transport process it becomes possible for high-energy electrons to survive to greater-than-expected distances from the pulsar, even when the magnetic field is large.

If electron escape is governed by Bohm diffusion, then the derived magnetic field leads to the coefficient $\kappa_{\text{Bohm}} = 1.8 \times 10^{23} E_{\text{TeV}} \text{ cm}^2 \text{ s}^{-1}$. However, the effect of escape losses are still negligible if $\kappa \lesssim 3.5 \times 10^{25} E_{\text{TeV}} \text{ cm}^2 \text{ s}^{-1}$. Although one can speculate whether this diffusion coefficient is large enough to allow for the X-ray electrons to survive to the edge of the nebula, this issue can ultimately only be addressed by solving the Fokker-Planck transport equation. Nevertheless, the large magnetic field derived may therefore still be consistent with observations.

The upper limit of the diffusion coefficient given in the previous paragraph can also be compared to the value $\kappa \sim 10^{27} E_{\text{TeV}} \text{ cm}^2 \text{ s}^{-1}$, or $\kappa = 2000\kappa_{\text{Bohm}}$, estimated by *Hinton et al.* (2011) for Vela X, and the value $\kappa = 3.1 \times 10^{26} E_{\text{TeV}} \text{ cm}^2 \text{ s}^{-1}$ derived by *Van Etten and Romani* (2011)

for HESS J1825–137. It is believed that both of these asymmetric PWNe have interacted with the reverse shock of a SNRs, and one may speculate that this has caused the initial toroidal magnetic field to develop a significant radial component, leading to effective diffusion along these field lines (*Van Etten and Romani, 2011*). By contrast, G21.5-0.9 is a young PWN with a toroidal magnetic field, and diffusion is therefore primarily perpendicular to the magnetic field. One would thus expect a diffusion coefficient that is smaller than those derived by *Hinton et al. (2011)* and *Van Etten and Romani (2011)*.

Other parameters derived for the nebula G21.5–0.9 include the ratio of conversion efficiencies $\eta_R/\eta_X = 5.7$, significantly smaller than the ratio $\eta_R/\eta_X = 116 - 150$ derived by *De Jager et al. (2008b)* for Vela X. The ratio of magnetic to particle energy is found to be $\sigma = 0.12$, larger than the value of $\sigma \sim 0.003$ calculated by *Kennel and Coroniti (1984b)* for the Crab Nebula. The well-known steady-state MHD model of *Kennel and Coroniti (1984a)* predicts a radial velocity that is almost independent of r when $\sigma = 0.25$. Based on this result, (4.14) should be a reasonable approximation for the adiabatic losses when $\sigma = 0.12$, as the velocity in the largest part of the PWN will not differ significantly from the expansion velocity. Note that these values are also comparable to the values derived by *Vorster et al. (2013b)* for a scenario with $\bar{B}_{\text{age}} = 230 \mu\text{G}$.

To illustrate the effect of a continuous/discontinuous source spectrum on the derived parameters, one need only consider the modelling results of *Tanaka and Takahara (2011)*. Using a continuous source spectrum and a model similar to the present one, these authors were unable to predict the 1 – 10 keV X-ray observations, while the present model with the different normalisation constants provides a very good description of the broadband spectra.

Following the discussion presented in Section 2.3.3, the non-thermal emission from G21.5–0.9 is also modelled using a Maxwellian spectrum with a power-law tail

$$Q(E_e, t) = \begin{cases} Q_T (E_e/E_{\text{ts}}) \exp[-E_e/E_{\text{ts}}], & \text{for all } E_e \\ Q_N \exp[(-E_e - E_{\text{max}})/\Delta E_{\text{max}}] (E_e/E_{\text{ts}})^{-\alpha_N}, & \text{if } E_b < E_e \leq E_{\text{max}} \end{cases}, \quad (4.21)$$

where Q_T and Q_N respectively represent the normalisation constants for the thermal and non-thermal components, and $E_{\text{ts}} = 0.26(\gamma/10^6)$ TeV. Here γ represents the Lorentz factor of the electrons upstream of the termination shock, while $E_b = 7E_{\text{ts}}$. Note that (4.21) is a slightly modified *Spitkovsky (2008)* spectrum introduced by *Fang and Zhang (2010)*. In contrast to the single normalisation constant used by *Fang and Zhang (2010)*, (4.21) again allows one to specify a normalisation constant for both the low- and high-energy components. The aim is not to model G21.5–0.9 time-dependently using (4.21), but merely to determine whether a Maxwellian spectrum can be used to explain the radio/GeV data.

Figure 4.2 shows that (4.21) can also be used to model the broadband data, except at radio frequencies where a much harder spectrum is predicted. From this modelling values for E_{min} and E_{max} are derived that are similar to the values listed in Table 4.2. Other parameters that are derived include a Lorentz factor of $\gamma = 6 \times 10^4$, implying a break energy of $E_b = 0.1$ TeV,

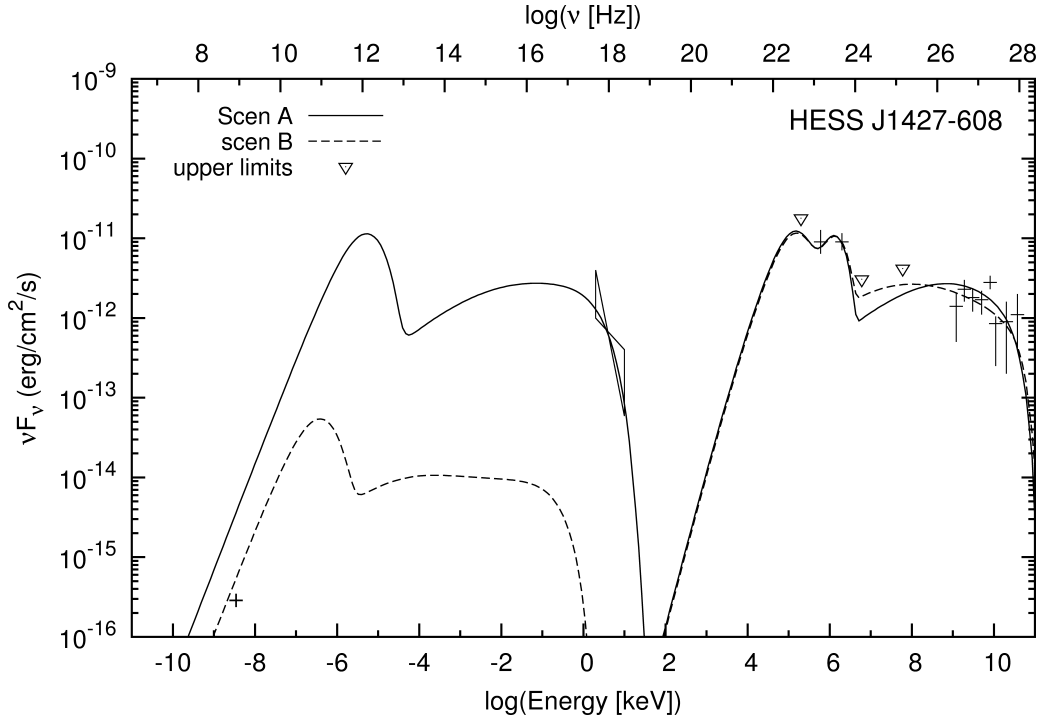


Figure 4.3: Model prediction for the unidentified source HESS J1427–608. The radio data are taken from *Murphy et al.* (2007), the X-ray data from *Fujinaga et al.* (2012), the *Fermi* data from *Nolan et al.* (2012), and the TeV data from *Aharonian et al.* (2008). For this source, the GeV/TeV spectrum is produced by the IC scattering of both the CMBR and an IR component.

along with $\alpha_N = 2.7$ and $\Delta E_{\max} = 160$ TeV for the power-law tail. These last two values are comparable to the values of $\alpha_N = 2.5$ and $\Delta E_{\max} = 100$ TeV predicted by *Spitkovsky* (2008).

4.3.3 HESS J1427–608

One of the sources discovered in a H.E.S.S. Galactic Plane Survey is HESS J1427–608, with an intrinsic source extension of $2'.4 - 4'.8$ (*Aharonian et al.*, 2008). Observations by *Fermi*-LAT detected an associated GeV source, 2FGL J1427.6–6048 (*Nolan et al.*, 2012), while *Fujinaga et al.* (2012) recently reported an X-ray detection with *Suzaku* in the 2 – 10 keV band. The X-ray emission is spatially coincident with the TeV emission, and has a radius of $2'$. Based on the well-known fact that the VHE nebula is typically larger than the X-ray nebula (see, e.g., *Kargaltsev and Pavlov*, 2010), it was suggested by *Fujinaga et al.* (2012) that the *Suzaku* observation represents the X-ray counterpart to HESS J1427–608. Using the X-ray observations, *Fujinaga et al.* (2012) estimated that the source is located at a distance of $d \sim 11$ kpc, and has an age of $t_{\text{age}} \sim 6.4$ kyr. A possible radio counterpart, MGPS J142755-605038 with a radius of $0'.56 - 0'.77'$, has been observed in a Molonglo Sky Survey (*Murphy et al.*, 2007). As the radio nebula of a PWN is typically larger than the X-ray nebula (see, e.g., *Gaensler and Slane*, 2006), it is difficult to simultaneously associate both the radio and *Suzaku* sources with the VHE emission, assuming that HESS J1427–608 is indeed a PWN, and that the *Suzaku* detection represents the X-ray nebula.

This incompatibility is also strongly underlined by the model.

For modelling purposes the value estimated by *Fujinaga et al. (2012)* is used as the age of the source. For a ~ 6 kyr source it is entirely possible that the PWN has not yet interacted with the reverse shock, and it is thus assumed that HESS J1427–608 is still in the first expansion phase. A number of scenarios were investigated, from which it followed that they all require the IC scattering of both the CMBR and an IR component in order to predict the GeV/TeV data. Placing the source at the distance estimated by *Fujinaga et al. (2012)*, *Vorster et al. (2013b)* required that an IR component with an energy density of $U_{\text{IR}} = 2 \text{ eV cm}^{-3}$ be included in the model. However, at a distance of $d = 11 \text{ kpc}$ the energy density of the IR field in the galactic plane is an order of magnitude smaller, i.e., $U_{\text{IR}} = 0.2 \text{ eV cm}^{-3}$ (*Strong et al., 2000*). As the energy density of the IR field increases towards the Galactic centre, this requirement of an IR component can be met by decreasing the distance to HESS J1427–608 in the model. The value for the distance was chosen to be as close as possible to the value of $d = 11 \text{ kpc}$, and it was found that a distance of $d = 8 \text{ kpc}$, where the energy density is $U_{\text{IR}} = 0.6 \text{ eV cm}^{-3}$ (*Strong et al., 2000*), makes it possible for the model to predict the correct GeV flux. The observed size and chosen distance lead to a radius of $R_{\text{pwn}} = 5.6 \text{ pc}$. The derived index of expansion is $r_1 = 0.98$, leading to present-day expansion velocity of $V_{\text{age}} = 835 \text{ km s}^{-1}$.

With adiabatic losses included, the model requires an initial luminosity of $L_0 = 8 \times 10^{39} \text{ erg s}^{-1}$ in order to predict the GeV and TeV data. As discussed in Section 4.3.1, L_0 determines the number of electrons in the nebula, with a larger value leading to more electrons and consequently a larger non-thermal photon flux. On the hand, adiabatic losses lead to a decrease in the intensity of the photon spectra, and the very large L_0 value can thus be reduced by neglecting this energy loss process. This is motivated by the fact that all the scenarios investigated require $\sigma \lesssim 10^{-3}$. Figure 3.4 in Section 3.3.4 shows that the radial velocity profile decreases as $V \propto 1/r^2$ if $\sigma < 10^{-2}$. It follows from (4.13) that the electrons will not be subjected to adiabatic losses for such a profile, thereby motivating the neglect of this energy loss process in the modelling.

As a single set of parameters could not fit both the radio and X-ray measurements, two scenarios were investigated. Figure 4.3 shows the model predictions, with the parameters listed in Table 4.2. Both scenarios presented in Figure 4.3 require a large initial luminosity ($L_0 = 9 \times 10^{38} \text{ erg s}^{-1}$) and spin-down time scale ($\tau = 3 \text{ kyr}$), leading to a present-day luminosity of $L = 9.2 \times 10^{37} \text{ erg s}^{-1}$.

From the first scenario a present-day magnetic field of $\bar{B}_{\text{age}} = 3.7 \mu\text{G}$ is derived. The ratio of electron conversion efficiencies is $\eta_{\text{R}}/\eta_{\text{X}} = 15.5$. Moreover, the model predicts that the ratio of magnetic to particle energy is $\sigma = 2 \times 10^{-4}$.

Even though the values derived for this first scenario are compatible with PWN parameters, the over-prediction of the radio data makes it difficult to accept this scenario. A bright radio source is predicted that has thus far not been observed in the region of the sky spatially coincident with the position of HESS J1427–608. A model prediction compatible with the radio

data can be obtained from the scenario presented above, provided that the minimum electron energy is $E_{\min} > 0.1$ TeV. This seems an unnaturally high value, and this solution is therefore not favoured.

For the second scenario presented in Figure 4.3 the present-day magnetic field has been reduced to $\bar{B}_{\text{age}} = 0.22 \mu\text{G}$, leading to a significantly better agreement between the model prediction and radio data. To make this scenario comparable to the $\bar{B}_{\text{age}} = 3.2 \mu\text{G}$, most of the parameters are left unchanged. The most notable difference is the very small ratio $\sigma = 10^{-6}$. This is needed in order to reduce the magnetic field to $\bar{B}_{\text{age}} = 0.22 \mu\text{G}$, although it is not excluded that a different scenario can produce a similar prediction using a larger σ value.

To understand why the model has difficulty in predicting both the radio and X-ray synchrotron data, one need only consider the two quantities that eventually determine the synchrotron flux: the number of electrons that produce the non-thermal emission, and the magnetic field strength. If the magnetic field is the same for both the radio and X-ray producing electrons, the only way to predict both the radio and X-ray data would be to increase the number of high-energy electrons. However, it follows from Figure 4.1 that this would also increase the TeV flux, leading to a predicted intensity that would be higher than the H.E.S.S. data.

This discrepancy between the two scenarios can possibly be explained if the low- and high-energy components are not spatially coincident, with the former component located in a region with a low magnetic field, and the latter component located in a region with a higher magnetic field. This would make HESS J1427–608 similar to the Vela PWN, where it has been observed that the two electron components are also not spatially coincident (*Grondin et al., 2013*). Alternatively, this discrepancy could also be explained if the *Suzaku* measurement is not the X-ray counterpart of HESS J1427–608.

Although the model contains a number of free parameters, it is nevertheless possible to some degree to delimit the parameter space: (1) the model requires that a significant number of electrons be present in the source, leading to large initial luminosities ($L_0 \gtrsim 5 \times 10^{38} \text{ erg s}^{-1}$) and spin-down time scales $\tau \sim 3000 \text{ yr}$; (2) an IR component must be included to predict the correct flux for the IC spectrum; (3) the ratio of electromagnetic to particle energy must be small ($\sigma < 10^{-3}$); and, (4) in order to predict the X-ray data requires an average magnetic field of $\bar{B}_{\text{age}} \sim 3 \mu\text{G}$, while the radio data requires a magnetic field of $\bar{B}_{\text{age}} \sim 0.3 \mu\text{G}$.

Although a small σ value is derived, it is difficult to make a quantitative analysis of this source using the HD simulations presented in Chapter 3. However, the small σ value does serve as a motivation for further investigation into the nature of HESS J1427–608 using the HD model, and such a future investigation is thus planned.

4.3.4 HESS J1507–622

Also discovered in a H.E.S.S. Galactic Plane Survey is the bright ($\sim 8\%$ of the Crab flux) and extended (a radius of $\sim 9'$) VHE source HESS J1507–622 (*Acero et al., 2011*). A possible synchro-

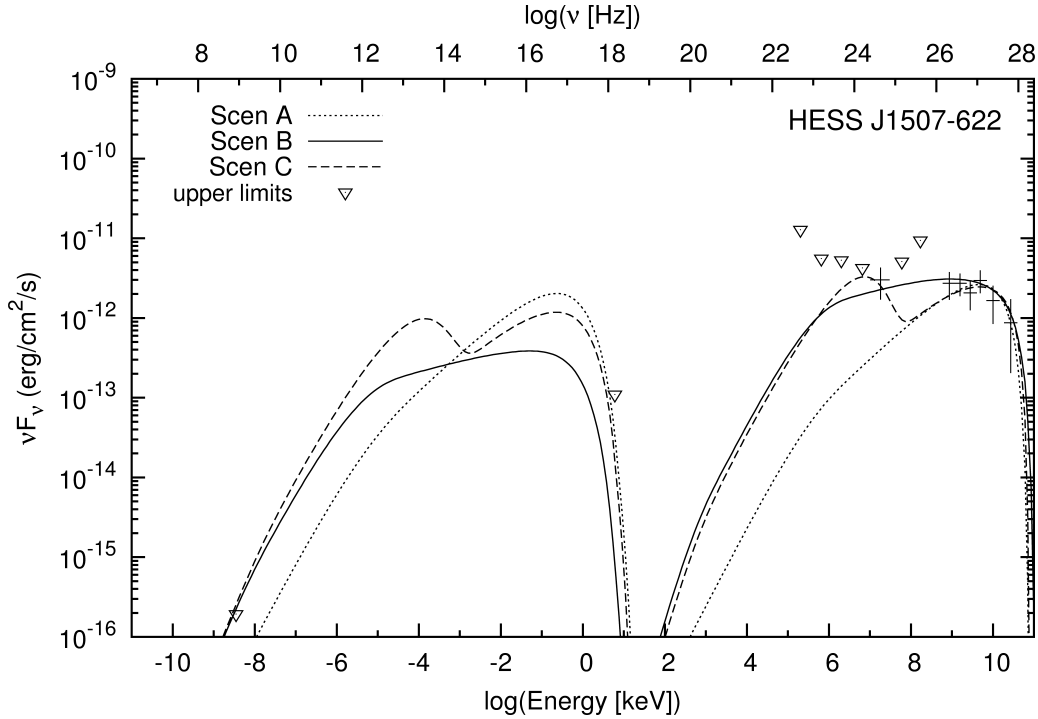


Figure 4.4: Model prediction for the unidentified source HESS J1507–622. The radio upper limit is taken from *Green et al.* (1999), and the GeV data from *Nolan et al.* (2012) and *Acero et al.* (2013). The X-ray upper limit and the TeV data are taken from *Acero et al.* (2011). The IC spectrum is produced by taking into account only the scattering of CMBR photons.

tron counterpart may be provided by the extended, diffuse X-ray emission (with a radius of $10'' - 13''$) observed with *Chandra* (*Acero et al.*, 2011). However, the identification of this X-ray source with the VHE emission region remains inconclusive (*Acero et al.*, 2011). An additional synchrotron upper limit is provided by the source MGPS J150850-621025 discovered in a Molonglo Galactic Plane Survey (*Green et al.*, 1999). Lastly, a GeV counterpart, 2FGL J1507.0-6223, has also been detected by the *Fermi* collaboration (*Nolan et al.*, 2012; *Acero et al.*, 2013).

HESS J1507–622 is unique in the sense that it lies $\sim 3^\circ.5$ from the Galactic plane, whereas all other unidentified sources lie within $\pm 1^\circ$ from the Galactic equator. Most Galactic VHE sources are associated with young stellar populations (located in the disk), and one would therefore not expect a bright VHE source at the observed position unless the source is nearby. Furthermore, the absence of a bright X-ray counterpart is surprising, as the comparably low hydrogen column density at $\sim 3^\circ.5$ leads to a considerably lower absorption of X-rays, as well as reduced background emission (*Acero et al.*, 2011).

To explain the uniqueness of the source, *Acero et al.* (2011) considered a number of possible scenarios. On the one hand, the absence of counterparts, especially in X-rays, suggests a hadronic scenario. Given the low density of target material off the Galactic plane (see, e.g., *Lockman*, 1984), this scenario was disfavoured by *Acero et al.* (2011). Although unlikely, the hadronic scenario can not be fully excluded (*Acero et al.*, 2011). One possibility is that HESS J1507–622 is

a nearby ($d \lesssim 2$ kpc) and young ($t \lesssim 1000$ yr) SNR. As argued by *Acero et al.* (2011), this would imply an SNR with characteristics similar to that of SN 1006. However, SN 1006 is a bright non-thermal X-ray source (see, e.g., *Koyama et al.*, 1995; *Willingale et al.*, 1996), and the absence of X-ray emission from HESS J1507–622 makes this scenario unlikely (*Acero et al.*, 2011). An alternative scenario is that HESS J1507–622 is an ancient PWN. As a result of its small angular extension, the leptonic scenario would place the source at a distance of $d > 6$ kpc (*Acero et al.*, 2011).

In their initial analysis of HESS J1507–622 the *Fermi* collaboration published data and upper limits that extended down to an energy of $E = 0.3$ GeV. However, in their second publication the data only extend down to $E = 20$ GeV (*Acero et al.*, 2013). Furthermore, the two data sets for $E \geq 20$ GeV are not completely in agreement. Therefore, for energies $E < 20$ GeV the upper limits published by *Nolan et al.* (2012) are used together with the data published by *Acero et al.* (2013) for higher energies. For the X-ray data the possible diffuse emission detected by *Chandra* is taken as an upper limit. As the latest GeV data does not require a discontinuous spectrum, the modelling will be done with a continuous spectrum, unless explicitly stated otherwise.

For the first scenarios investigated it is assumed that HESS J1507–622 is still in the initial expansion phase. In Section 3.3.1 it was shown that the outer radius of the PWN evolves as $R_{\text{pwn}}(t) \propto t^{1.1} - R_{\text{pwn}}(t) \propto t^{1.3}$, similar to the time-dependence $R_{\text{pwn}}(t) \propto t^{1.2}$ derived by *Reynolds and Chevalier* (1984). This latter time-dependence is also adopted in the modelling of HESS J1507–622. The source is placed at a distance of $d = 6$ kpc, leading to a radius of $R_{\text{pwn}} = 15.7$ pc. With the chosen expansion index and size of the PWN, (4.15) leads to an age of $t_{\text{age}} = 4.6$ kyr and an expansion velocity of $V_{\text{age}} = 4000$ km s $^{-1}$. Although the latter value is much larger than the values derived for G21.5–0.9 ($V_{\text{age}} = 1060$ km s $^{-1}$) and HESS J1427–608 ($V_{\text{age}} = 835$ km s $^{-1}$), it is nevertheless used for the modelling, but it will also be discussed how a larger age influences the results.

The results from the various scenarios investigated are shown in Figure 4.4, with the derived parameters listed in Table 4.3. It will be recalled from (4.2) that the spectral index of the high-energy component of the electron injection spectrum is chosen as $N_e \propto E_e^{-2}$. However, it is immediately clear from the results (Scen A) that such a spectrum cannot predict the GeV data. In order to obtain a reasonable prediction, as shown in Scen B, the high-energy component must be described by the spectrum $N_e \propto E_e^{-2.7}$. For this scenario an initial luminosity of $L_0 = 4 \times 10^{38}$ erg s $^{-1}$ is derived, together with a spin-down time scale of $\tau = 2500$ kyr. The ratio of magnetic to particle energy is $\sigma = 10^{-3}$, leading to a present-day average magnetic field of $\bar{B}_{\text{age}} = 1$ μ G.

As energy-dependent escape losses can lead to a softening of the electron spectrum, it is possible to obtain a prediction similar to the one shown for Scen B by using $N_e \propto E_e^{-2}$ and $\kappa = 100\kappa_{\text{Bohm}}$. For this scenario a larger spin-down time scale is required ($\tau = 3000$ kyr), while the initial luminosity ($L_0 = 5 \times 10^{38}$ erg s $^{-1}$), ratio of particle to magnetic energy ($\sigma = 10^{-3}$), and present-day magnetic field ($\bar{B}_{\text{age}} = 1.2$ μ G) is similar to that of Scen B.

To investigate the effect of the age of the nebula on the results, simulations were also performed using the larger value $t_{\text{age}} = 9$ kyr. Based on the results of Section 3.3.1, it is highly likely that the PWN would already have interacted with the reverse shock of the SNR. However, Figure 3.1 shows that compression does not start immediately, but is delayed by a few thousand years. With this larger age the expansion index and velocity decrease to the values $r_1 = 1.082$ and $V_{\text{age}} = 1850 \text{ km s}^{-1}$, respectively. It was found that, using the same parameters as listed in Table 4.3 for Scen B, the larger age leads to a model prediction that is very similar to that of Scen B. In both scenarios the escape time scales are larger than the ages of the systems, while the weak magnetic fields derived generally lead to synchrotron loss time scales that are also larger than the ages of the systems. Lastly, as the largest fraction of energy is injected into the nebula when $t \ll \tau$, the energy content of the two systems should be comparable. It thus follows that the age of the system will not necessarily influence the modelling results.

Alternatively, one can also investigate how the distance estimate influences the results. In this scenario the source is placed at a distance of $d = 3$ kpc, implying a PWN with a radius of $R_{\text{pwn}} = 7.9$ pc. The expansion index is again chosen to be $r_1 = 1.2$. Inserting these values into (4.15) leads to an age of $t_{\text{age}} = 2.6$ kyr and an expansion velocity of $V_{\text{age}} = 3570 \text{ km s}^{-1}$. A model prediction similar to Scen B is obtained using $L_0 = 10^{38} \text{ erg s}^{-1}$, $\tau = 2.5$ kyr and $\sigma = 4 \times 10^{-6}$. This leads to a present-day magnetic field of $\bar{B}_{\text{age}} = 1 \mu\text{G}$. Note that all other parameters not discussed are similar to those listed for Scen B in Table 4.3.

As the expansion velocity in the previous scenario is again larger than that derived for G21.5–0.9 and HESS J1427–608, a scenario with $d = 3$ kpc and an expansion index of $r_1 = 1.02$, similar to the value derived for G21.5–0.9 in Section 4.3.2, was also investigated. These values lead to an age of $t_{\text{age}} = 6.9$ kyr and an expansion velocity of $V_{\text{age}} = 1140 \text{ km s}^{-1}$. A model prediction similar to Scen B is obtained using $L_0 = 10^{38} \text{ erg s}^{-1}$, $\tau = 2.5$ kyr and $\sigma = 4 \times 10^{-6}$ (similar to the $r_1 = 1.2$, $d = 3$ kpc scenario). This leads to a present-day magnetic field of $\bar{B}_{\text{age}} = 1.2 \mu\text{G}$. The only difference between these scenarios is that the IC spectrum for the present scenario begins to deviate from that of Scen B at 0.1 TeV, leading to an intensity that is a factor two lower at 10 TeV.

Using the initial *Fermi*-LAT data (Nolan *et al.*, 2012), Vorster *et al.* (2013b) found that a continuous spectrum could not predict the GeV data, while a discontinuous spectrum required a break energy of $E_b = 5$ TeV. This value for E_b is an order of magnitude larger than the values derived for G21.5–0.9 ($E_b = 0.12$ TeV) and HESS J1427–608 ($E_b = 0.18$ TeV). Values similar to those presented in Table 4.2 have also been derived for a number of known PWNe, including the ~ 21 kyr old nebula HESS J1825–137. Zhang *et al.* (2008) found that $E_b \leq 0.15$ TeV, comparable to the values of $E_b \leq 0.3$ TeV derived by Tanaka and Takahara (2011). The exception to the modelling results of Tanaka and Takahara (2011) is Kes 75, where the authors derived a possible value of $E_b = 2.6$ TeV. Using a Maxwellian source spectrum, Fang and Zhang (2010) derived the even smaller values of $E_b = 0.02 - 0.09$ TeV.

As adiabatic heating will cause the electron spectrum to shift to higher energies, Vorster *et al.*

(2013b) suggested that the large value required for E_b can possibly be explained if the PWN has been compressed by the reverse shock of the SNR. Although a discontinuous spectrum is no longer required by the latest *Fermi*-LAT data, the compression scenario is nevertheless still investigated. In order to constrain the scenario to some degree, the HD simulations presented in Section 3.3 are used as guidelines, with the acknowledged caveat that these simulations are only valid if $\sigma < 0.01$. Figure 3.1 shows that the nebula is only significantly compressed if $L_0 \lesssim 10^{38} \text{ erg s}^{-1}$, or if $\tau \sim 0.5 \text{ kyr}$. In these scenarios the compression of the PWN starts at $t \sim 9 \text{ kyr}$, with this phase lasting $\lesssim 10 \text{ kyr}$.

As an illustrative example of a compression scenario, consider a PWN that initially expands for $t = 9 \text{ kyr}$ at a rate of $r_1 = 1.1$ (as predicted by the HD simulations), eventually reaching a size of $R_{\text{pwn}} = 18 \text{ pc}$. Given the offset from the Galactic plane, it seems reasonable to assume that the ISM is homogeneous. This will lead to a symmetric reverse shock and a preservation of the spherical nature of the PWN. The compression phase lasts for $t = 5 \text{ kyr}$, with the final size of the PWN being equal to the observed size of $R_{\text{pwn}} = 15.7 \text{ pc}$. The model prediction for this scenario is shown in Figure 4.4 (Scen C), with the derived parameters listed in Table 4.3. As one would not expect any photon field other than the CMBR to be present at the position of HESS J1507–622, only this component is taken into account when calculating the IC spectrum.

A large initial luminosity $L_0 = 8 \times 10^{38} \text{ erg s}^{-1}$, together with a small spin-down time scale $\tau = 0.3 \text{ kyr}$ is derived. In this regard the derived results is to some degree comparable to the HD simulations as a large L_0 is required in order for the PWN to reach a size of $R_{\text{pwn}} = 18 \text{ pc}$. Furthermore, for such a large L_0 the spin-down time scale necessarily has to be small if the nebula is to be significantly compressed. Other parameters derived include the ratios $\eta_R/\eta_X = 7.2$ and $\sigma = 9 \times 10^{-3}$, and the present-day average magnetic field $\bar{B}_{\text{age}} = 1.9 \mu\text{G}$.

Even with the latest *Fermi*-LAT data, a break energy of $E_b = 5 \text{ TeV}$ is still required if the PWN has not been compressed by the reverse shock of the SNR. With the compression taken into account, the break energy is reduced to $E_b = 0.5 \text{ TeV}$. Note that this is the break energy of the source spectrum, while the electron spectrum in the PWN has a break at 5 TeV . Furthermore, adiabatic heating also causes the value of E_{min} , as listed under Scen C of Table 4.3, to shift to a higher energy in the nebula. While the model is able to predict the data, one of the difficulties of this scenario is that the adiabatic heating predicted by (4.14) has to be artificially increased by an order of magnitude. It should, however, be kept in mind that (4.14) is not necessarily the best approximation for adiabatic losses. Furthermore, Scen C is just an example of a possible compression scenario, and it is therefore not excluded that other possible scenarios may also exist. A compression phase that lasts $t = 10 \text{ kyr}$ was also investigated, where it was found that this does not lead to a prediction that is significantly different than that of Scen C.

In conclusion, a prediction of the data does not require a discontinuous spectrum. Using a continuous spectrum large initial luminosities of $L_0 = 10^{38} - 5 \times 10^{38} \text{ erg s}^{-1}$ are derived, together with large spin-down time scales of $\tau = 2.5 - 3 \text{ kyr}$. Note that although Scen A requires a smaller L_0 , this scenario cannot predict the multi-wavelength data. One unifying feature

of all scenarios investigated, both continuous and discontinuous, is that a small present-day magnetic field of $\bar{B}_{\text{age}} \sim 2 \mu\text{G}$ is derived, larger than the value of $\bar{B}_{\text{age}} = 0.5 \mu\text{G}$ estimated by *Tibolla et al. (2011a)* and *Acero et al. (2011)*.

4.4 Summary

In this chapter a time-dependent PWN particle evolution model is presented and applied to the young PWN G21.5–0.9, as well as to the unidentified TeV sources HESS J1427–608 and HESS J1507–622. Sets of parameters are derived for the three sources that are reasonable within a PWN framework, thereby strengthening the argument that HESS J1427–608 and HESS J1507–622 may be identified as PWNe. As discussed by *Possenti et al. (2002)*, observations indicate that the X-ray luminosity of the PWN decreases with age, while *Mattana et al. (2009)* found that there is no correlation between the pulsar’s spin-down luminosity and the observed TeV luminosity of the PWN. The corollary is that the PWN will remain bright at TeV energies, even if the pulsar’s spin-down luminosity has decreased to an undetectable level. This evolutionary trend is also predicted by the model, as the synchrotron luminosity of the evolved PWNe fades away below the sensitivity of the current generation of X-ray satellites, while nevertheless remaining bright at TeV energies.

Apart from detecting pulsars that can be associated with the unidentified sources, additional multi-wavelength observations may further strengthen the PWN identification. A characteristic of PWNe is that electrons and positrons are responsible for the observed non-thermal emission. Although it will not directly confirm an unidentified TeV source as a PWN, the detection of a 511 keV annihilation line by future sub-MeV experiments, such as the proposed GRIPS satellite (*Greiner et al., 2012*), will at least indicate that the electrons responsible for the TeV emission in the unidentified sources are leptonic (*Tibolla et al., 2011b*).

As such, only a few alternative explanations for the unidentified TeV sources have thus far been proposed, including the suggestion by *Yamazaki et al. (2006)* that these sources can be associated with old SNRs. Arguing that SNRs can only confine multi-TeV particles for a very short period ($t \lesssim 1 \text{ kyr}$) the aforementioned suggestion has, however, been questioned by *Gabici and Aharonian (2007)*. As a second alternative, *Gabici and Aharonian (2007)* have suggested that the unidentified sources can still be identified with SNRs if escaped multi-TeV particles interact with nearby dense clouds. However, this scenario seems unlikely for the unidentified sources discovered so far, given the absence of dense molecular clouds spatially coincident with most of these sources. Given its location above the Galactic plane, this is particularly true for HESS J1507–622.

Motivated by observations, a broken power law is used as the source spectrum for the electrons injected into the PWN at the termination shock. In contrast to previous PWN models of a similar nature (see, e.g., *Zhang et al., 2008*; *Tanaka and Takahara, 2010*), the source spectrum in the present model allows for a discontinuity in intensity at the transition between the low

and high-energy components. For G21.5–0.9 and HESS J1427–608 a discontinuous spectrum leads to a significantly better agreement between the model and the multi-wavelength data, in contrast to a continuous one. A similar conclusion has also been drawn by *De Jager et al.* (2008b) from their modelling of Vela X. As a discontinuous spectrum is also required for the young ($t_{\text{age}} \sim 1$ kyr) nebula G21.5–0.9, the discrepancy between the two components cannot be an artefact of PWN evolution. A characteristic of the discontinuous spectrum is that a electron conversion efficiency must be specified for both the low (η_{R}) and high-energy (η_{X}) components, with a ratio of $\eta_{\text{R}}/\eta_{\text{X}} \sim 6 - 16$ derived for these two sources. By contrast, a better agreement between the model prediction and data is obtained for HESS J1507–622 using a continuous spectrum. It is important to note that a given spectrum was not favoured a priori, but that all sources were modelled using both a continuous and discontinuous spectrum.

The data for G21.5–0.9 were also modelled using a Maxwellian source spectrum with a non-thermal tail. The aim was not to model the evolution of the PWN time-dependently, but rather to illustrate that a Maxwellian source spectrum can be used to reproduce the observations. Although the Maxwellian spectrum supplies a natural explanation for the ratio $\eta_{\text{R}}/\eta_{\text{X}} > 1$, a synchrotron radio spectrum is predicted that is harder than the one observed. However, as discussed in Section 2.3.3, the results of *Sironi and Spitkovsky* (2011) indicate that magnetic reconnection at the termination shock can accelerate electrons, leading to a modification of the Maxwellian that would produce a softer radio synchrotron spectrum. It should however be noted that *Fang and Zhang* (2010) and *Grondin et al.* (2011) were able to model the non-thermal emission from a number of PWNe using a Maxwellian with a non-thermal tail.

Two possible scenarios were investigated for the candidate nebula HESS J1427–608. In the first, a present-day magnetic field of $B_{\text{age}} = 3.7 \mu\text{G}$ is derived. However, this scenario predicts a bright radio nebula that has thus far not been observed. An alternative scenario is considered where the magnetic field in the nebula has evolved to a very low value of $B_{\text{age}} = 0.3 \mu\text{G}$, leading to a synchrotron spectrum that is compatible with radio upper limits. However, this scenario significantly under-predicts the *Suzaku* observations presented by *Fujinaga et al.* (2012). The $B_{\text{age}} = 0.3 \mu\text{G}$ scenario represents an ancient PWN as the very small present-day magnetic field leads to a low level of synchrotron emission, while the PWN still remains bright at GeV/TeV energies. The fact that the model cannot simultaneously predict both the radio and X-ray observations could be explained if one of the two synchrotron sources is not a counterpart to HESS J1427–608. Alternatively, the radio/GeV emission and X-ray/TeV emission may be produced in two regions that are not spatially coincident, similar to what is observed for Vela X (*Grondin et al.*, 2013). Additionally, in order to fit both the radio and X-ray emission would require that the two regions have different magnetic field strengths.

Assuming that HESS J1507–622 is still in the initial expansion phase, the high-energy component of the electron injection spectrum requires a spectral index of $\alpha = 2.7$, in contrast to the value $\alpha = 2$ used for G21.5–0.9 and HESS J1427–608. Although it is possible for diffusive shock acceleration to produce such a soft spectrum, this could also be due to electrons effectively es-

caping from the nebula. It is also possible to model HESS J1507–622 with a discontinuous spectrum. However, this scenario requires that the energy value where the electron spectrum transitions from the low to high-energy components to be an order of magnitude higher than the values derived for G21.5–0.9, HESS J1427–608, and a number of other PWNe (e.g., *Zhang et al.*, 2008; *Fang and Zhang*, 2010; *Tanaka and Takahara*, 2011). Such a large value is possible if HESS J1507–622 has been compressed by the reverse shock of the SNR, with the resulting adiabatic heating leading to a larger break energy in the nebula. One noteworthy point is that a discontinuous scenario requires a ratio $\eta_R/\eta_X = 7.2$, comparable to the values derived for the other two sources modelled. Regardless of the scenario investigated, a present-day magnetic field of $B_{\text{age}} \sim 2 \mu\text{G}$ is derived. Furthermore, if the faint X-ray source is indeed the synchrotron counterpart to the VHE nebula, the present modelling results strengthens the argument for identifying HESS J1507–622 as a PWN.

It is reiterated that the model does not include a time-dependence in a number of parameters (e.g., η_R , η_X , E_b), and no comment can be made regarding the temporal evolution of the parameters listed in Table 4.2. However, the model does allow for the derivation of additional parameters, most notably the ratio η_R/η_X , that may be unique to PWNe. This requires that the current model be applied to a large number of known PWNe, allowing for the derivation of a statistically significant set of parameters.